Volume 55
Number 12
24 March 2026
Pages 4751-5078

Dalton Transactions

An international journal of inorganic chemistry

rsc.li/dalton

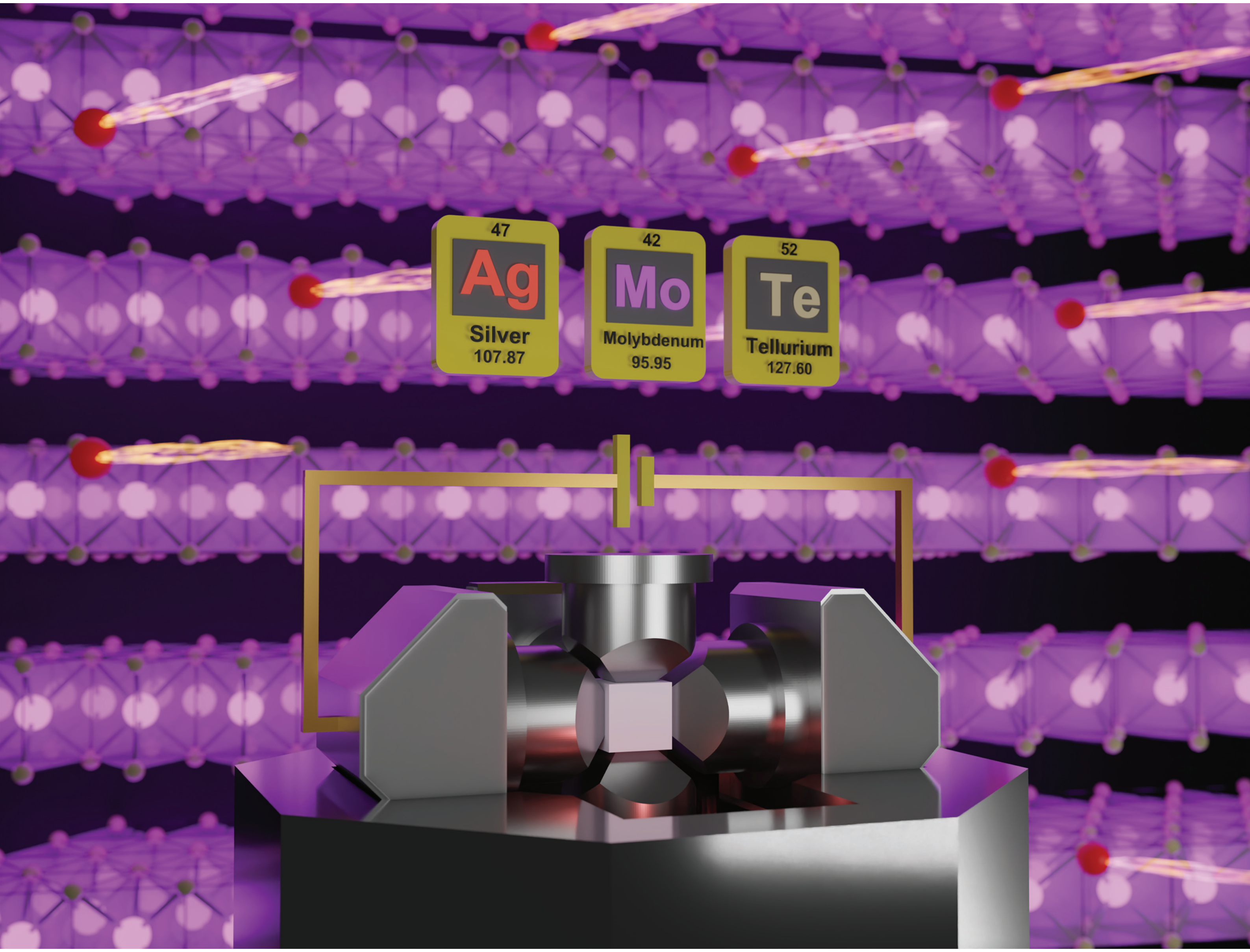

ISSN 1477-9226

ROYAL SOCIETY
OF **CHEMISTRY**

PAPER

Suguru Iwasaki, Masaya Fujioka *et al.*

Introduction of Ag ions into 2H-$MoTe_2$ *via* the high-pressure diffusion control method

Dalton Transactions

ROYAL SOCIETY OF CHEMISTRY

PAPER

View Article Online
View Journal | View Issue

Check for updates

Cite this: *Dalton Trans.*, 2026, **55**, 4772

Received 24th October 2025,
Accepted 19th February 2026

DOI: 10.1039/d5dt02554k

rsc.li/dalton

Introduction of Ag ions into 2H-$MoTe_2$ *via* the high-pressure diffusion control method

Suguru Iwasaki, *[a,b] Melbert Jeem, [c] Akitoshi Nakano [d] and Masaya Fujioka *[b,e]

Transition metal dichalcogenides (TMDs) are a major family of compounds for exploring functional materials through intercalation. In this study, the intercalation of Ag ions into 2H-$MoTe_2$ using the high-pressure diffusion control (HPDC) method was performed. Due to the application of high pressure (HP), 2H-$MoTe_2$ with a hexagonal lattice exhibited symmetry-lowered (HP-distorted) domains that can be indexed to a triclinic phase. Owing to the HPDC method, Ag ions were homogeneously distributed throughout the sample. This study opened a pathway for promoting ion introduction and achieving functional modulation in systems where intercalation was previously considered difficult, through a mechanism that is distinct from simple structural changes that merely elongate the interlayer space.

Introduction

Intercalation of ion species is one of the strategies to explore functional materials,[1–7] such as thermoelectric materials, superconductors, battery materials, catalysts, and optical materials. Transition metal dichalcogenides (TMDs) are a major family of compounds for exploring functional materials through intercalation. Among TMDs, the group VI TMDs have been intensively focused on because of the variety of polymorphs, particularly in nanoscale systems where short diffusion lengths and high defect densities facilitate ion insertion in the various contexts of thin films and electrochemistry.[8–11]

$MoTe_2$, a group VI TMD, exhibits polymorphism of 2H and 1T′ phases. The stable phase at 25 °C is the 2H phase with a hexagonal lattice (Fig. 1(a)).[11] Above 850 °C, the stable phase becomes the 1T′ phase with a monoclinic lattice (Fig. 1(b)), and the 1T′ phase can also be retained at room temperature as a metastable phase by quenching. Owing to the crystal field of $MoTe_6$ with the trigonal prismatic coordination, the 2H phase exhibits semiconducting behavior, while the 1T′ phase is metallic. Among these phases, the 2H phase is regarded as a promising thermoelectric material upon carrier doping. To date, hole doping by the partial substitution of Mo ($[Kr]4d^5 5s^1$) by Nb ($[Kr]4d^4 5s^1$) has been reported.[11,12] However, intercalation of ion species between layers in bulk scale has not been reported. In this context, the challenge lies in the intercalation process as a bulk-scale synthesis, with the objective of achieving uniform intercalation at the millimeter scale in crystalline group VI TMDs, while preserving long-range structural

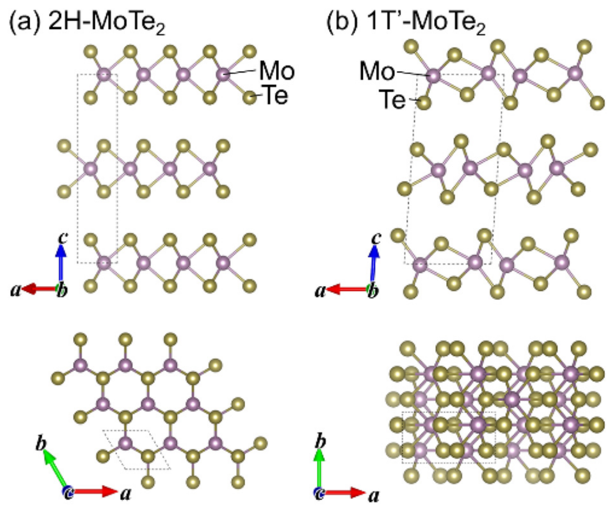

Fig. 1 Crystal structures of (a) 2H-$MoTe_2$ (hexagonal $P6_3/mmc$ space group, no. 194) and (b) 1T′-$MoTe_2$ (monoclinic $P21/m$ space group, no. 11). Dashed lines indicate the unit cells. The crystal structure was drawn using VESTA.[13]

---

[a] Department of Industrial Chemistry, Faculty of Engineering, Tokyo University of Science, Katsushika, Tokyo, 125-8585, Japan. E-mail: iwasaki.suguru@rs.tus.ac.jp
[b] Research Institute for Electronic Science, Hokkaido University, Kita 20, Nishi 10, Kita-ku, Sapporo, Hokkaido 001-0020, Japan
[c] Faculty of Engineering, Hokkaido University, Kita 13, Nishi 8, Kita-ku, Sapporo 060-8628, Japan
[d] Department of Physics, Nagoya University, Nagoya 464-8602, Japan
[e] Multi-material Research Institute, National Institute of Advanced Industrial Science and Technology (AIST), 4-205 Sakurazaka, Moriyama-ku, Nagoya, Aichi 463-8560, Japan. E-mail: m.fujioka@aist.go.jp

coherence. Such bulk-scale intercalation is considerably more difficult due to limited diffusion lengths, strain accumulation, and phase instability, which is why intercalation at this length scale has rarely been realized in experimental contexts.

A recently developed method called high-pressure diffusion control (HPDC) has enabled overcoming of these limitations and realized a bulk-scale intercalation. This allows a direct measurement of the bulk-scale functionality.

The HPDC method combines "intercalation and deintercalation processes"[14] with "high-pressure (HP) effects"[15] and can modulate the chemical composition while preserving the framework structure by effectively controlling ion diffusion.[16] This method is particularly effective when there is a large difference in bond strength between the diffusive ion species and the framework-forming elements. In the HPDC process, a stacking structure of three layers, "ion supplier/solid electrolyte/target material" for ion introduction and "target material/solid electrolyte/ion absorber" for ion extraction, is employed.

One notable example is the extraction of Na ions from $NaAlB_{14}$[17] *via* HPDC. $NaAlB_{14}$ consists of Na ions that are weakly trapped in the strong covalent framework of B. At approximately 550 °C, Na ions can diffuse through the B network, and by extracting Na ions, metastable AlB_{14}, which is not on the Al–B binary phase diagram, can be synthesized. HPDC has also been applied to ionic crystals, such as $BaTiO_3$, in which O^{2-} can diffuse under HPDC conditions around 650 °C while maintaining the framework of the perovskite structure.[18] In this way, HPDC is highly effective for topotactic reactions in compounds with large differences in bond strength. Layered compounds, which consist of weak van der Waals bonding between layers and strong covalent bonding within layers, represent a particularly promising target for this method. The application of HPDC to such systems is expected to broaden the range of accessible layered materials.

In general, chemical composition changes induced by introduction, extraction, or ion exchange inevitably cause lattice expansion or contraction. The resulting microscopic and macroscopic cracks can significantly degrade ion diffusivity and, in some cases, suppress the reaction itself. In addition, the lattice strain introduced by these processes may severely deteriorate the crystallinity of the material. In contrast, the HPDC process applies external pressure to suppress mechanical damage and chemical degradation associated with volume changes, thereby facilitating smooth reaction progression. As a result, samples processed *via* HPDC exhibit high sintering density and robust intergranular connectivity, making them well suited for evaluating intrinsic bulk transport properties.

In this study, Ag ions were selected as intercalants for $2H\text{-}MoTe_2$ among monovalent cations that readily intercalate as electron dopants. This selection was based on the higher stability of the resulting compound compared to those formed with alkali metal ions. As a result, microscopic HP-distorted (symmetry-lowered) domains of $MoTe_2$ were observed after the high-pressure process (indexed by FFT/diffraction spot geometry), and their thermoelectric properties were evaluated.

Experiments

The entire synthetic procedure is shown in Fig. 2(a).

Sample preparation

Polycrystalline $2H\text{-}MoTe_2$ powder was prepared by a solid-state reaction using an evacuated quartz tube. Mo powder (99.9 wt%, Fujifilm) and Te lump (99.99 wt%, Fujifilm) were ground, and the mixture was pelletized. The pellet was sintered in an evacuated quartz tube at 750 °C for 20 hours, and then cooled at ∼20 °C in the furnace. HP annealing for the obtained as-grown sample was performed using multi-anvil pressure apparatus at a temperature (T) from 400 °C to 450 °C with a ramp rate of 2 °C h^{-1} under 1 GPa for 25 h.

Introduction of Ag ions *via* HPDC

Introduction of Ag ions was performed using the HPDC method. The HPDC setup is illustrated in Fig. 2(b). A 2 : 1 mixture of Ag (99.9 wt%, Sigma-Aldrich, Japan) and AgI (99.9 wt%, Fujifilm) in a molar ratio was utilized as a source of Ag ions. The pellets of the as-grown sample, AgI (solid electrolyte), and the Ag–AgI mixture (ion supplier) were stacked and installed into a pressure cell. HPDC treatment was performed using multi-anvil pressure apparatus at T from 400 °C to 450 °C with a ramp rate of 2 °C h^{-1} under 1 GPa for 25 h.

Characterization and evaluation

The as-grown, HP, and HPDC samples were characterized using synchrotron X-ray diffraction (XRD) with λ = 0.71992 Å on a BL5S2 experimental station in the Aich Synchrotron Radiation Center. The elemental composition was determined

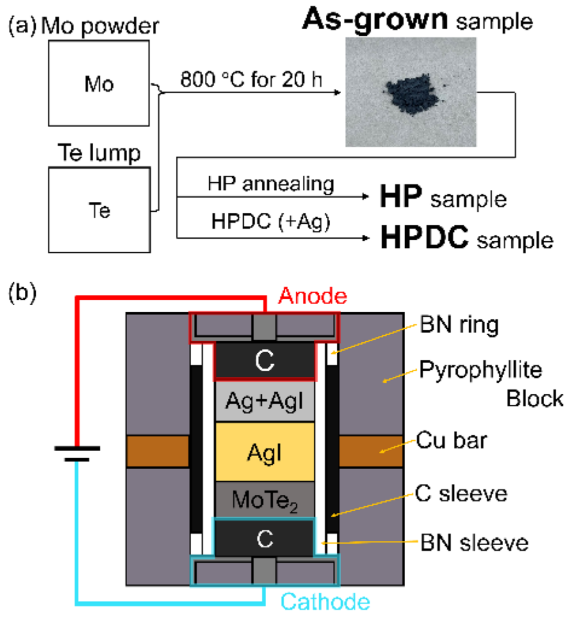

Fig. 2 (a) Schematic of the synthetic procedure of the as-grown, HP, and HPDC samples. (b) The experimental setup of an HPDC cell for the synthesis of Ag-introduced $MoTe_2$.

using an energy-dispersive X-ray spectroscopy (EDS) instrument (MP-00040EDAD, Jeol) attached to a secondary-electron microscope (SEM) (JCM-6000, Jeol). The valence state was analyzed using X-ray photoelectron spectroscopy (XPS) (JPS-9200, Jeol). Transmission electron microscopy samples were prepared by mechanical exfoliation and dropped onto a perforated amorphous carbon film supported on a Cu microgrid (EM Japan, Co., Ltd). Dark-field TEM and high-angle annular dark-field (HAADF) scanning TEM (STEM) images were acquired using a JEOL NEOARM 200F (equipped with a Cs corrector) combined with a cold-field emission gun operated at 80 kV. The beam current was nominally 33 pA to prevent electron beam-induced damage. The electrical resistivities (ρ) of the HP and HPDC samples were measured by a four-probe method at T between 5 and 300 K. Seebeck coefficients (S) and total thermal conductivities (κ_{total}) were measured under steady-state conditions.

Results and discussion

Effect of HP annealing on 2H-$MoTe_2$

Fig. 3 shows synchrotron XRD patterns for the as-grown and HP samples (before and after HP annealing, respectively). All the peaks were assigned to the 2H phase of $MoTe_2$. Lattice constants of the as-grown and HP samples were a = 0.351906 nm, c = 1.396230 nm and a = 0.351854 nm, c = 1.396540 nm with a hexagonal lattice, respectively. After HP annealing, a decreased by 0.02% and c increased by 0.03%. These differences indicated that HP annealing did not significantly affect the crystal structure of 2H-$MoTe_2$. On the other hand, the intensity of the HP sample was 41.8% of that of the as-grown sample. Additionally, the full width at half maximum (FWHM) of the maximum peak at 16.2° for the HP sample was 0.075°, whereas that for the as-grown sample was 0.036°. To clarify the cause of the peak broadening, analysis based on the Williamson–Hall plot was performed for each sample (Fig. S1 and Table S1). This analysis revealed that HP annealing enhanced the crystallite size, which generally resulted in peak narrowing. This inconsistency between the experimental peak broadening and the peak narrowing, suggested by the crystallite size analysis, can be explained by the lattice strain. When the contribution of crystallite size and lattice strain to the peak broadening was separated (Fig. S2), the lattice strain accounted for approximately 70% of peak broadening in the HP sample, whereas 20% in the as-grown sample. Additionally, in the HP sample, several $\beta_\varepsilon/\beta_T$ values were higher than the rest and they originated from (00l) peaks. Thus, HP annealing deformed the 2H phase and the lattice strain was primarily applied to the c-axis. The results of the XRD analysis were found to be in close agreement with the distortions of the β and γ angles that were observed in the FFT spot analysis. This indicated that HP annealing introduced anisotropic lattice distortion in the 2H phase.

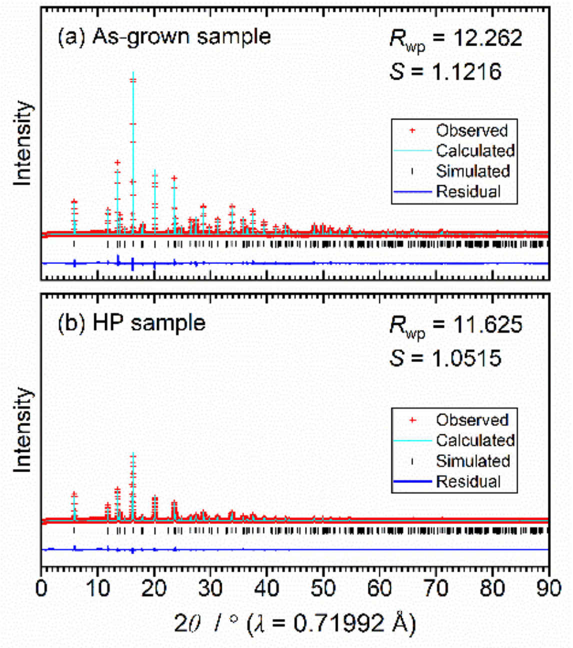

Fig. 3 Synchrotron XRD patterns (a) before and (b) after HP annealing.

In TEM images of the HP sample (Fig. 4), two distinct local lattice metrics were observed. Area 1 shows the hexagonal reciprocal geometry consistent with the dominant 2H matrix in near-[001] plan-view. In contrast, the diffraction pattern observed for area 2 is markedly different from that of the 2H phase, making it difficult to directly infer the structure from the 2H lattice. We therefore examined a model based on the known 1T′ structure viewed along the c-axis and introduced a triclinic distortion. Specifically, when the monoclinic lattice angles were modified to β = 98.6° and γ = 100°, an excellent agreement was obtained with the diffraction spots observed for the HP phase. In this model, the fractional atomic coordinates were taken directly from the reported 1T′ structure, and only the lattice angles were varied. This triclinic phase is considered an intermediate state during the phase transition from the 2H to the 1T′ phase, characterized by a reduction of the γ angle from 120° toward 90° (observed as around 100°) and a tilting of the β angle from the ideal 90°. These distortions contribute to the decrease in intensity and the increase in FWHM in the synchrotron XRD patterns. The intermediate phase generated by HP annealing from the 2H phase is referred to as "the HP phase" in this paper.

Thus, although the HP sample was composed of both the 2H and HP phases, as revealed by the TEM analysis, only the 2H phase was detected in the synchrotron XRD. Its lattice parameters remained unchanged, but the peak intensity was reduced to approximately half. This significant decrease in intensity is likely due to a reduced mass fraction of the 2H phase resulting from the partial conversion to the HP phase. As for the absence of clear diffraction peaks from the HP phase in the synchrotron XRD, the following three explanations are tentatively proposed and discussed as possible reasons:

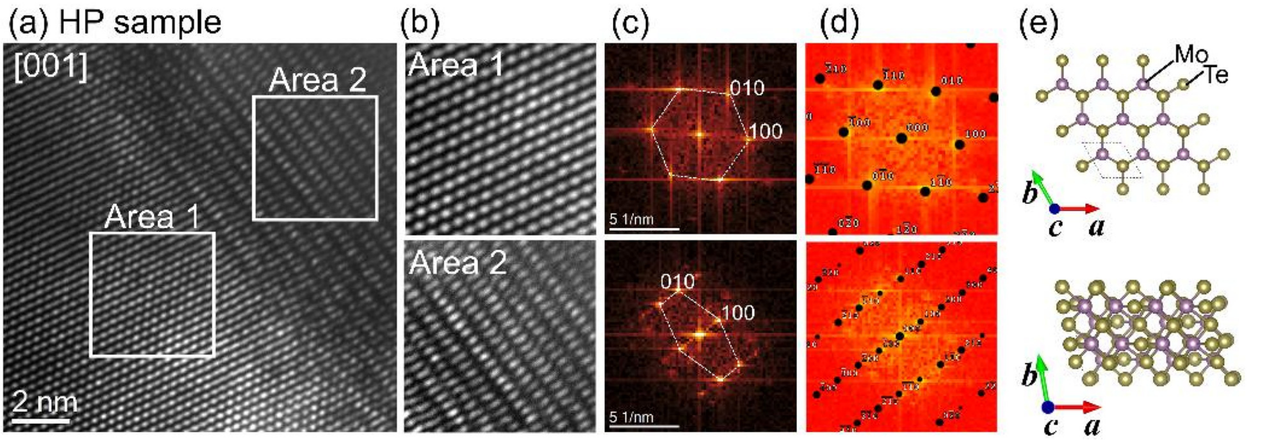

Fig. 4 (a) TEM images of the HP sample. (b) Expanded views of area 1 and area 2. (c) FFT patterns of areas 1 and 2. (d) Simulated [001]-zone electron diffraction patterns (black markers; indexed) overlaid on the experimental FFT intensity maps for Area 1 (upper; 2H) and Area 2 (lower; triclinic). (e) The corresponding crystal structures based on the FFT patterns ([001] view direction).

(1) Low symmetry of the triclinic lattice: the triclinic lattice exhibits low symmetry among crystal systems, leading to an increased number of diffraction peaks and decreased intensity for each individual peak. In particular, since the distortions along two axes are allowed in a triclinic lattice, the structure may vary continuously, resulting in peak broadening and potential overlap with the background.

(2) Sub-nanoscale domains of the HP phase: TEM observations revealed that the HP phase locally appears on a sub-nano scale. Generally, a nano-scale morphology, such as nano particles, shows peak broadening even in synchrotron XRD. Similarly, slight structural variations across different domains in the HP phase are expected to result in broadening of the diffraction peaks, making them difficult to distinguish from the background.

(3) Low volume fraction of the HP phase: the 2H phase remains the dominant phase after HP treatment. The limited volume fraction of the HP phase, combined with its broadened diffraction peaks, may result in an intensity too weak to be detected by XRD.

These factors are consistent with our TEM/FFT observations of localized HP domains and with the Williamson–Hall analysis, indicating strain-dominated broadening.

Introduction of Ag ions into 2H-MoTe$_2$ *via* HPDC

The total electricity passed (Q_{pass}) calculated from the time–current profile during the HPDC process (Fig. S3) was 42.5 C, which was sufficient for the expected electricity (Q_{exp}) of 29.5 C required to obtain Ag$_x$MoTe$_2$ with x = 1.0 ($Q_{\text{exp}}/Q_{\text{pass}}$ = 1.44 (>1.00)). The voltage decreased to 0.05 V with increasing temperature up to 400 °C, and subsequently, the voltage increased to 0.08 V during heating with a ramp rate of 2 °C h^{-1}. After 16.9 h, noise in the voltage was observed. The total charge passed by 16.9 h was 30.4 C.

In the EDS mapping of Ag (Fig. 5), Ag ions were distributed homogeneously from the AgI side to the C side, and their aggregation was not observed. In the EDS spectra, Ag peaks were obviously confirmed. Quantitatively, the amount of x in Ag$_x$MoTe$_2$ was 0.15 (AgI side), 0.11 (middle) and 0.10 (C side), respectively, although x was estimated to be more than 1.00 from the current profile. This indicated that most of the current that occurred during the HPDC process was due to the flow of electrons, rather than the migration of Ag ions.

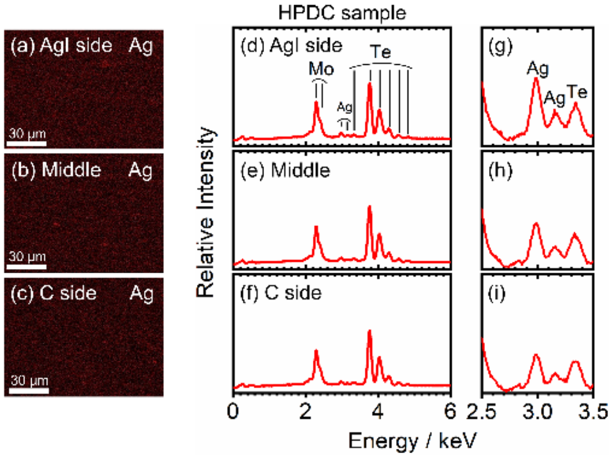

Fig. 5 EDS mapping and spectra of the cross-sectional areas for the HPDC sample during SEM observation. (a–c) Elemental mapping of Ag for the upper (near the AgI side), middle, and bottom (near the C side) areas. (d–f) EDS spectra and (g–i) expanded views of (d–f) between 2.5 and 3.5 keV.

Fig. 6 shows the XPS spectra of Ag, AgI, and HPDC samples. The peak of Ag-3d$_{5/2}$ in the HPDC sample was observed at 367.91 eV, which was different from those of Ag$_2$Te at ~368.2 eV.[19] Additionally, the peak of Ag-3d$_{5/2}$ in the HPDC sample was lower than those of AgI (368.05 eV) and Ag (368.23 eV). This indicated that the density of electrons around Ag in the HPDC sample was almost identical to that in AgI and lower than that in Ag, confirming that Ag in the HPDC sample is in an ionic state.

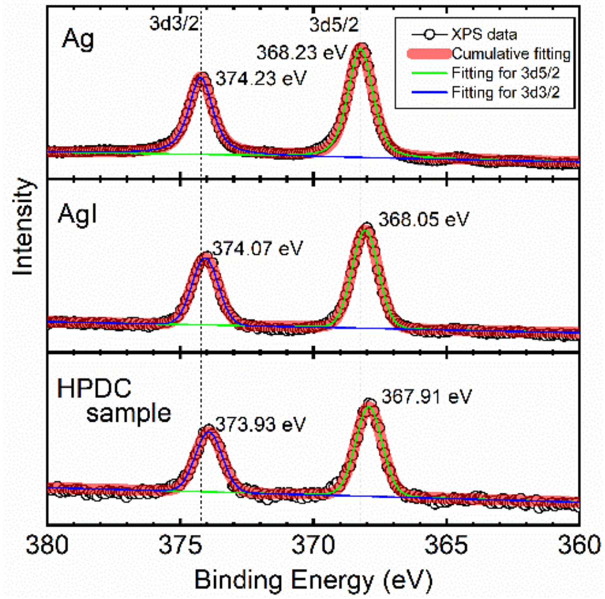

Fig. 6 XPS spectra of Ag-3$d_{3/2}$ and 3$d_{5/2}$ orbitals for Ag, AgI, and HPDC samples.

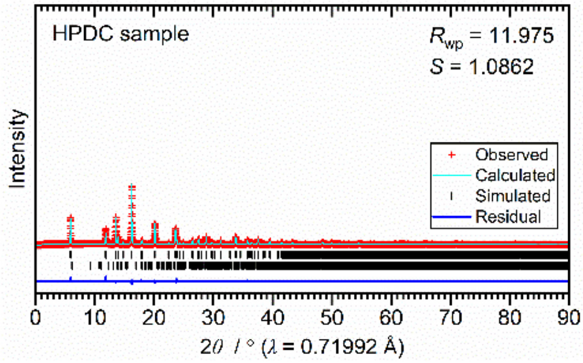

Fig. 7 Synchrotron XRD patterns of the HPDC sample.

In the synchrotron XRD pattern (Fig. 7), the HPDC sample contained 99 wt% of 2H phase and 1 wt% of Ag_2Te. The lattice parameters of the 2H phase were a = 0.351868 nm and c = 1.396520 nm, which were similar values of the as-grown and HP samples, indicating that Ag ions were not introduced into the 2H phase. Additionally, the FWHM of the maximum peak at 16.2° was 0.080° and this peak broadening was mainly caused by the lattice strains due to the Williamson–Hall plot (Fig. S1 and Table S1). It is noted that 1 wt% of Ag_2Te corresponds to ~0.01 as x, and the peak of Ag-3$d_{5/2}$ for the HPDC sample was different from that for Ag_2Te in the XPS spectra. Thus, most of the Ag ions detected by EDS and XPS were from Ag_xMoTe_2 and not from Ag_2Te.

To identify the phase into which Ag ions were introduced, TEM observation was conducted (Fig. 8). Three different phases were confirmed. For area 1, the hexagonal lattice was observed, which corresponded to the 2H phase as observed in the XRD patterns. For area 2, the distorted lattice where γ was 100° was observed. This phase is suggested to be an intermediate state of the phase transition from the 2H phase to the HP phase (HP′ phase). For area 3, the FFT spot geometry can be indexed to an HP-distorted (triclinic-metric) lattice showing a supercell feature (a-axis doubling) and $\beta \approx 98.6°$. These phase developments are schematically summarized using the energetically stable structures obtained by relaxing atomic positions *via* first-principles calculations under fixed unit cell geometry conditions (Fig. 8(c)). Because the HAADF contrast is sensitive to thickness/tilt and the present data do not uniquely constrain Ag atomic coordinates, we do not assign a specific Ag crystallographic site from STEM data alone and instead present a lattice-metric/indexing model supported by simulated diffraction patterns. The exact position of the Ag ions should be investigated further. The absence of clear diffraction peaks from areas 2 and 3 in the synchrotron XRD patterns can tentatively be explained by similar reasons to the case of HP annealing, as mentioned in (1)–(3).

Thermoelectric properties of the HPDC sample

Fig. 9 shows the thermoelectric properties of the HP and HPDC samples. These thermoelectric properties were affected by phase inhomogeneity: 2H phase and HP phase with no Ag ions for the HP sample and 2H phase and Ag-introduced HP phase for the HPDC sample. Considering the phase compositions between the HP and HPDC samples, the difference in thermoelectric properties was attributed to the Ag introduction.

The HP sample exhibits a semiconductive dependence of resistivity on the temperature and its Seebeck coefficient was positive under 290 K and negative above 290 K. The resistivity and Seebeck coefficient indicated that the HP sample was a multi-carrier semiconductor with holes and electrons as carriers. A typical 2H phase exhibits $\sim 10^4$ Ω cm electrical resistivity and −800 μV K^{-1} Seebeck coefficient at 300 K,[12] whereas those for the HP sample were 10^2 Ω cm and −40 μV K^{-1}. The change in the Seebeck coefficient indicated the increase in electrons as carriers, and thus, the electrical resistivity decreased. These results indicated that HP annealing induced electron doping for the 2H phase. A possible cause of electron doping by HP annealing is the defect of Te ($Te^{2-} \rightarrow Te + 2e^-$) in the HP sample. This effect is expected to appear in the HPDC sample. A small amount of Ag_2Te observed in the XRD analysis might result from the reaction between the defective Te and introduced Ag ions. The electrical resistivity for the HPDC sample was also semiconductive. However, the resistivity of the HPDC sample was 10^{-5}–10^{-2} times lower than that of the HP sample, which indicated that the carrier density increased due to Ag introduction. The Seebeck coefficient of the HPDC sample was negative for the whole range of temperature, and thus, the majority carrier in the HPDC sample was electrons. This was in agreement with the theoretical expectation that the introduction of Ag corresponds to the doping of

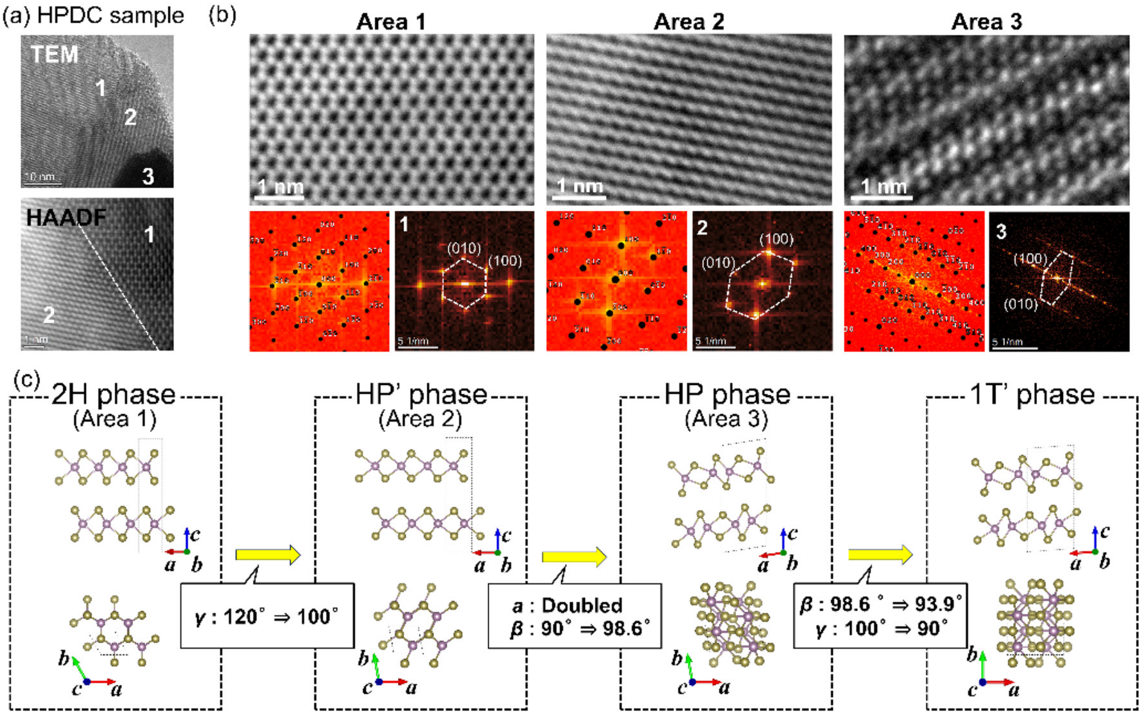

Fig. 8 (a) Dark-field TEM and HAADF-STEM images of the HPDC sample. (b) Expanded view with the corresponding FFT patterns and overlaid simulated TEM diffraction patterns on the FFT spots. (c) Phase development from the 2H phase to the 1T′ phase of the $MoTe_2$ framework.

electrons ($Ag \rightarrow Ag^+ + e^-$), indicating that Ag ions were introduced into $MoTe_2$. Owing to the electron doping, the decrease in electrical resistivity and increase in the Seebeck coefficient were realized simultaneously.

In contrast to the resistivity and Seebeck coefficient, total thermal conductivities were similar in HP and HPDC samples. Based on the Wiedemann–Franz law, the electronic thermal conductivity (κ_{electron}) was found to be less than 0.002 W m^{-1} K^{-1} for both the HP and HPDC samples (Fig. S4). Considering that the κ_{total} is composed of κ_{electron} and lattice thermal conductivity (κ_{lattice}), most of the κ_{total} is influenced by the lattice because the contribution of κ_{electron} to κ_{total} was less than 0.03% even at 300 K. In this context, there was no significant change in the lattice between HP and HPDC samples, and thus, the small difference in thermal conductivity was reasonable. In addition, the HP sample exhibited 7 W m^{-1} K^{-1} thermal conductivity at 300 K, whereas the typical 2H phase exhibited 12.5 Wm^{-1} K^{-1} at 300 K.[12] In the HP and HPDC samples, the 2H and HP phases exhibited a decrease in crystallinity during the process of phase transition from the 2H to HP phase. The decrease in crystallinity enhanced phonon scattering, which led to a decrease in the thermal conductivity of the HP and HPDC samples. Therefore, the formation of the HP phase resulted in the reduction of thermal conductivity. Additionally, in the HPDC sample, Ag introduction, while maintaining the framework, led to an increase in electrical conduction.

The figure of merit (ZT) (Fig. S5), which is $S^2T/\rho\kappa$, for the HP sample exhibited a valley at 290 K where the sign of the

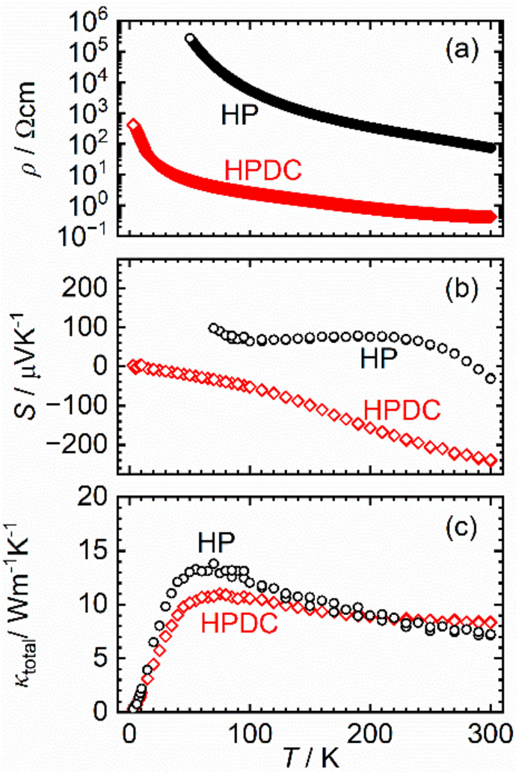

Fig. 9 Thermoelectric properties of HP and HPDC samples. (a) Resistivity (ρ), (b) Seebeck coefficient (S), and (c) total thermal conductivity (κ_{total}).

Seebeck coefficient was reversed. The *ZT* of the HPDC sample was enhanced by 10^3–10^4 times since the electrical resistivity and Seebeck coefficient were enhanced while maintaining the thermal conductivity by Ag introduction. At 300 K, Nb-substituted $MoTe_2$ ($Mo_{1-y}Nb_yTe_2$) with $y = 0.07$ exhibits *ZT* of 0.025,[12] which is 250 times higher than that of the HPDC sample. In the HPDC sample, the Seebeck coefficient was 1.6–2.2 times higher than that of $Mo_{1-y}Nb_yTe_2$, whereas the electrical resistivity was 10^6 times higher. This higher resistivity caused a low *ZT*.

Conclusions

In this study, the introduction of Ag ions into 2H-$MoTe_2$ under high pressure *via* the HPDC method was performed. Owing to the HPDC method, Ag ions were homogeneously distributed throughout the sample. Although 1 wt% of Ag_2Te was observed as a secondary phase, the chemical state of Ag ions was clearly different from that in Ag_2Te, and thus most of the Ag ions were introduced into $MoTe_2$.

From the viewpoint of crystal structure, HP/HPDC introduces local symmetry-lowering distortions and disorder consistent with a shear-type pathway toward 1T′-like stacking, while Ag introduction modulates electronic transport without requiring large lattice expansion. To realize the macroscopic phase homogeneity, the synthetic condition through the HPDC process should be optimized further. However, this study showed the potential for functional modulation by introducing Ag ions *via* HPDC.

This study opened a pathway for promoting ion introduction and achieving functional modulation in systems where intercalation was previously considered difficult, through a mechanism that is distinct from simple structural changes that merely elongate the interlayer space.[18]

Author contributions

S. I.: methodology, validation, investigation, resources, writing – original draft, writing – review & editing, visualization, project administration, and funding acquisition. M. J.: validation, formal analysis, investigation, resources, writing – review & editing, and funding acquisition. A. N.: validation, formal analysis, investigation, resources, and writing – review & editing. M. F.: conceptualization, methodology, resources, writing – original draft, writing – review & editing, supervision, project administration, and funding acquisition.

Conflicts of interest

There are no conflicts to declare.

Data availability

The data supporting this article have been included as part of the supplementary information (SI). Supplementary information: the Williamson–Hall plots for the synchrotron XRD patterns, the current profile during the HPDC process, the electronic thermal conductivity, and the dimensionless figure of merit (*ZT*) of the HP and HPDC samples. See DOI: https://doi.org/10.1039/d5dt02554k.

Acknowledgements

This work was supported by the Japan Science and Technology Agency (JST) CREST (Grant No. JPMJCR19J1), the Japan Society for the Promotion of Science (JSPS) (Grant No. JP19H02420, JP24K01171, JP24K01593 and JP24K01588), and the Murata Science and Education Foundation.

References

1 J. Zhou, Z. Lin, H. Ren, X. Duan, I. Shakir, Y. Huang and X. Duan, *Adv. Mater.*, 2021, **33**, 2004557.
2 Y. Luo, J. Yang, G. Li, M. Liu, Y. Xiao, L. Fu, W. Li, P. Zhu, J. Peng, S. Gao and J. Zhang, *Adv. Energy Mater.*, 2013, **4**, 1300599.
3 K. Zagarzusem, M. Fujioka, T. Shibuya, S. Demura, S. Adachi, Y. Takano, M. Jeem, M. Ono, H. Kaiju and J. Nishii, *2D Mater.*, 2020, **8**, 015007.
4 M. S. Whittingham, *Prog. Solid State Chem.*, 1978, **12**, 41–99.
5 W. Bao, J. Wan, X. Han, X. Cai, H. Zhu, D. Kim, D. Ma, Y. Xu, J. N. Munday, H. D. Drew, M. S. Fuhrer and L. Hu, *Nat. Commun.*, 2014, **5**, 4224.
6 J. Yao, K. J. Koski, W. Luo, J. J. Cha, L. Hu, D. Kong, V. K. Narasimhan, K. Huo and Y. Cui, *Nat. Commun.*, 2014, **5**, 5670.
7 M. Fujioka, K. Zagarzusem, S. Iwasaki, A. Sharma, K. Watanabe, R. Nakayama, M. Momai, Y. Yamaguchi, H. Shimada, K. Nomura, Y. Mizutani, H. Sumi, M. Tanaka, M. Jeem, M. Hattori, H. Saitoh, T. Ozaki, M. Nagao and K. Nagashima, *J. Am. Chem. Soc.*, 2024, **146**, 34324–34332.
8 X. C. Liu, S. Zhao, X. Sun, L. Deng, X. Zou, Y. Hu, Y. X. Wang, C. W. Chu, J. Li, J. Wu, F. S. Ke and P. M. Ajayan, *Sci. Adv.*, 2020, **6**, eaay4092.
9 H. Zhang, A. Rousuli, S. Shen, K. Zhang, C. Wang, L. Luo, J. Wang, Y. Wu, Y. Xu, W. Duan, H. Yao, P. Yu and S. Zhou, *Sci. Bull.*, 2020, **65**, 188–193.
10 S. Xu, K. Evans-Lutterodt, S. Li, N. L. Williams, B. Hou, J. J. Huang, M. G. Boebinger, S. Lee, M. Wang, A. Singer, P. Guo, D. Y. Qiu and J. J. Cha, *ACS Nano*, 2024, **18**, 17349–17358.
11 M. Wang, S. Xu and J. J. Cha, *Adv. Energy Sustainability Res.*, 2021, **2**, 2100027.

12 C. Zhang, Z. Li, M. Zhang, Z. Li, H. Sang, S. Xie, Z. Wang, H. Xie, J. Luo, W. Wang, H. Ge, Y. Liu, Y. Yan, W. Liu and X. Tang, *J. Solid State Chem.*, 2021, **300**, 122227.

13 K. Momma and F. Izumi, *J. Appl. Crystallogr.*, 2011, **44**, 1272–1276.

14 S. Iwasaki, H. Morito, T. Komine, K. Morita, T. Shibuya, J. Nishii and M. Fujioka, *Adv. Mater.*, 2022, **34**, 2106754.

15 S. Iwasaki, M. Hoshino, H. Morito, M. Kumagai, Y. Katsura, J. Nishii and M. Fujioka, *Solid State Sci.*, 2023, **144**, 107308.

16 M. Fujioka, M. Hoshino, S. Iwasaki, H. Morito, M. Kumagai, Y. Katsura, K. Zagarzusem, M. Ono and J. Nishii, *Chem. Mater.*, 2023, **35**, 3008–3014.

17 S. Iwasaki, M. Hoshino, H. Morito, M. Kumagai, Y. Katsura, M. Jeem, M. Ono, J. Nishii and M. Fujioka, *Inorg. Chem.*, 2022, **61**, 4378–4383.

18 M. Fujioka, *JSAP Rev.*, 2025, **2025**, 250402.

19 E. K. Kim, D. Park, N. K. Shrestha, J. Chang, C. W. Yi and S. H. Han, *Dalton Trans.*, 2016, **45**, 17312–17318.